Article:
Wang, Z, Yang, Y, Lu, N et al. (2 more authors) (2019) Effects of the principal stress rotation in numerical simulations of geotechnical laboratory cyclic tests. Computers and Geotechnics, 109. pp. 220-228. ISSN 0266-352X

https://doi.org/10.1016/j.compgeo.2019.01.023

Effects of the Principal Stress Rotation in Numerical Simulations of Geotechnical Laboratory Cyclic Tests

Zhe Wang[1,2,*], Yunming Yang[3], Nan Lu[2], Yao Li[4], Hai-Sui Yu[5]

1 Department of Civil Engineering, Faculty of Engineering, University of Lishui, Lishui 323000, China

2 Department of Civil Engineering, International Doctoral Innovation Centre, University of Nottingham, Ningbo 315100, China

* Corresponding Author: Department of Civil Engineering, Faculty of Engineering, Lishui University, Lishui 323000, China; P. +86 18867859227 Email. wangzhe@lsu.edu.cn

3 Department of Civil Engineering, Ningbo Nottingham New Materials Institute, University of Nottingham, Ningbo 315100, PR China

4 *School of Highway, Chang'an University, Xi'an* 710064, China

5 School of Civil Engineering, University of Leeds, Leeds LS2 9JT, UK

Abstract

Cyclic stress paths in geotechnical experiments can generate considerable principal stress rotation (PSR) in the saturated soil. The PSR without changes of principal stress magnitudes can generate additional excess pore water pressures and plastic strains, thus accelerating liquefactions in undrained conditions. This paper simulates a series of laboratory tests considering the PSR using two types of sand. The impact of PSR is taken into account by using an elastoplastic soil model developed on the basis of a kinematic hardening soil model with the bounding surface concept. The soil model considers the PSR by treating the stress rate generating the PSR independently. The capability of this soil model is verified by comparing the numerical predictions with and without PSR, as well as experimental results. The comparative results indicate that the simulation with the soil model considering the PSR can better reproduce the test results on the development of shear strain, reduction of effective confining pressure and liquefaction than the soil model without PSR. Therefore, it is important to consider PSR effects in simulations of geotechnical experiments under cyclic loadings.

KEYWORDS: soil elastoplastic model; principal stress rotation; liquefaction; cyclic loading; numerical simulation

1. Introduction

The soil behavior under cyclic loadings, such as earthquake loadings and wave loadings, is one of the major research areas in both numerical simulations and experimental studies. It

is more complex than soil behavior under monotonic loadings because the soil is subjected to considerable and repetitive rotation of principal stress axes, in addition to the change in principal stress magnitudes. Ishihara & Towhata [1] found that this principal stress rotation (PSR) alone, i.e without a change of principal stress magnitudes, can generate plastic deformations and the non-coaxiality in soils. The PSR can also generate excess pore water pressures and plastic strains in undrained conditions. Similar phenomenon is also found by a number of researchers [2-6]. It is well established that the additional excess pore water pressure and plastic deformation caused by the PSR from cyclic loadings can accelerate undrained soil liquefaction. Ignoring the PSR impact may lead to unsafe designs.

The non-coaxial and PSR behavior of soil have been explored numerically by numerous models based on different theories, such as yield vertex model [7], hypoplastic models [8, 9], multi-laminate models [10], multi-mechanism model [11], extended platform model [12], double shearing models [13], microplane model [14], and unified hardening model [15-17]. However, most of these models basically focus on the non-coaxiality and did not account for the pure PSR impact. In 1993, Gutierrez et al. [18] proposed an elastoplastic kinematic hardening model based on experimental studies. It can consider the rotational loading and the volumetric strain induced by the PSR, thus simulating the PSR behaviors under cyclic loadings and liquefactions of undrained sands. However, its numerical implementations can be complicated because its elastoplastic stiffness matrix is a function of the stress increment, thus leading to the nonlinear relationship between the stress and strain increments.

This paper aims to take into account the effect of PSR on soil behaviors in numerical simulations of a series of experimental tests by using a well established PSR model. This model is developed on the basis of a kinematic hardening model with the bounding surface and critical state concept. The PSR soil model considers the PSR effect by treating the stress rate generating the PSR independently. The model has been partly validated in single element studies with Toyoura sand [19]. The results show that this model has the potential to simulate the PSR effects in single element studies. The focus of the paper is on the investigation of PSR impacts under cyclic loadings with more complete single element simulations using Leighton Buzzard sand and Nevada sand. Firstly, the original base model and the modified PSR model will be introduced. Secondly, these two models will be tested in a series of single element numerical simulations of experimental tests with various types of sands. Finally, the comparison will be made between results from the original base model, the modified PSR model and the experimental tests to detailly distinguish the strong and weak points of the PSR theory.

2. The Original Soil Model

A well-established soil model with the bounding surface concept and kinematic hardening is chosen as the base model. It employs the critical state concept, the principle of phase transformation line, the back-stress ratio as the hardening parameter and the state parameter to represent influences of different confining stresses and void ratios on sand behaviors. However, it does not give special consideration of PSR effects. This model will be briefly introduced and more details can be found in Dafalias & Manzari [20].

The yield function of the model is defined as:

$$f = [(\mathbf{s} - p\boldsymbol{\alpha}) : (\mathbf{s} - p\boldsymbol{\alpha})]^{1/2} - \sqrt{2/3}\, pm = 0 \quad (1)$$

where **s** is the deviatoric stress tensor. p and **α** are the confining pressure and back-stress ratio tensor, respectively. **α** represents the center of yield surface in the stress ratio space while m is the radius of yield surface. The normal to the yield surface is defined as:

$$\mathbf{l} = \frac{\partial f}{\partial \boldsymbol{\sigma}} = \mathbf{n} - \frac{1}{3}(\mathbf{n}:\mathbf{r})\,\mathbf{I}; \qquad \mathbf{n} = \frac{\mathbf{r}-\boldsymbol{\alpha}}{\sqrt{2/3}\, m} \quad (2)$$

where **I** is the isotropic tensor and **n** represents the normal to the yield surface on the deviatoric plane. **r** represents the stress ratio and is equal to **s** / p. The elastic deviatoric strain rate $d\mathbf{e}^e$ and volumetric strain rate $d\varepsilon_v^e$ are defined as:

$$d\mathbf{e}^e = d\mathbf{s} / 2G \quad (3)$$

$$d\varepsilon_v^e = dp / K \quad (4)$$

The plastic strain rate $d\boldsymbol{\varepsilon}^p$ is defined as:

$$d\boldsymbol{\varepsilon}^p = \langle L \rangle \mathbf{R} \quad (5)$$

$$L = \frac{1}{K_p}\left(\frac{\partial f}{\partial \boldsymbol{\sigma}}\right) : d\boldsymbol{\sigma} \quad (6)$$

$$\mathbf{R} = \mathbf{n} + \frac{1}{3} D\,\mathbf{I} \quad (7)$$

where L represents the loading index and **R** is the direction of the plastic strain rate. K_p is the plastic modulus and D is the dilatancy ratio and they are defined as:

$$K_p = \frac{2}{3} p\left[G_0 h_0 (1 - c_h e)\left(\frac{p}{p_{at}}\right)^{-1/2}\right]\left[\frac{|\mathbf{b} : \mathbf{n}|}{|(\boldsymbol{\alpha} - \boldsymbol{\alpha}_{in}) : \mathbf{n}|}\right] \quad (8)$$

$$D = A_d\, \mathbf{d} : \mathbf{n} \quad (9)$$

where **b** and **d** are the distances between the current back-stress ratio tensor and bounding and dilatancy back-stress ratio tensors, respectively. h_0, c_h and A_d are the model parameters. $\boldsymbol{\alpha}_{in}$ is the initial value of **α** at the start of a new loading process and is updated when the denominator becomes negative.

3. The Modified PSR Soil Model

A brief introduction of the modified PSR model is given here and detailed description can be found in Yang & Yu [19]. In the modified model, the plastic strain rate is split into the monotonic strain rate $d\boldsymbol{\varepsilon}_m^p$ and the PSR induced strain rate $d\boldsymbol{\varepsilon}_r^p$, where the subscript m and r represent monotonic and PSR loading hereinafter, respectively. This treatment of separation only applies to the derivation of plastic strain rates, and the evolution of hardening parameter is not affected. Therefore, the plastic strain rate can be expressed as:

$$d\boldsymbol{\varepsilon}_m^p = \langle L_m \rangle \mathbf{R}_m = \frac{1}{K_{pm}} \left(\frac{\partial f}{\partial \boldsymbol{\sigma}} d\boldsymbol{\sigma}_m\right) \mathbf{R}_m \tag{10}$$

$$d\boldsymbol{\varepsilon}_r^p = \langle L_r \rangle \mathbf{R}_r = \frac{1}{K_{pr}} \left(\frac{\partial f}{\partial \boldsymbol{\sigma}} d\boldsymbol{\sigma}_r\right) \mathbf{R}_r \tag{11}$$

It is assumed that $K_{pm} = K_p$ and $\mathbf{R}_m = \mathbf{R}$ (equations 7 & 8) because the original model is for the non-PSR loading. The direction of PSR strain rate $\mathbf{R}_r$ can be expressed as:

$$\mathbf{R}_r = \mathbf{n}_r + \frac{1}{3} D_r \mathbf{I} \tag{12}$$

where $\mathbf{n}_r$ is the direction of deviatoric plastic strain rate and can be approximated as $\mathbf{n}$ for simplicity. D_r is the dilatancy ratio for the PSR loading rate, it can be derived from the postulate of the PSR dilatancy ratio of Gutierrez et al. [5] and expressed as:

$$D_r = A_r (1 - \alpha/\alpha^b_\theta)\, \alpha \tag{13}$$

where A_r is a constant for the impact of PSR on dilatancy. However, this equation has a shortcoming, especially under the drained condition. Petalas et al. [22] pointed out that during the simulation of drained PSR loading, if the sample is initially denser than critical, the value of α^b_θ (already being larger than α) will increase due to its dependence on the state parameter (Dafalias & Manzari [20]), as the sample becomes denser under the PSR induced contraction, rendering the D_r always larger than 0. Thus, the model predicts an endless volumetric contraction as long as the PSR continues, which is physically unacceptable. Similar problem was circumvented in Li & Dafalias [12] and Lashkari & Latifi [21] by rendering the PSR dilatancy a decreasing function of the cumulative shear strain. Petalas et al. recently proposed an approach by reformulating the conventional dilatancy expression (i.e. Equation 9) to include a densification function. This function includes a new hardening parameter that evolves only in the case of non-coaxiality and tends to zero the dilatancy ratio at large cycles [22]. In the current paper, the Equation 13 is kept without modifications in order to preserve its simple and elegant theoretical basis.

The plastic modulus K_{pr} for PSR loading rate is defined as:

$$K_{pr} = \frac{2}{3} p \left[G_0 h_{0r} (1 - c_h e) \left(\frac{p}{p_{at}} \right)^{-1/2} \right] \left(\frac{|\mathbf{b} : \mathbf{n}|}{|(\boldsymbol{\alpha} - \boldsymbol{\alpha}_{in}) : \mathbf{n}|} \right)^{\xi_r} \tag{14}$$

where h_{0r} and ξ_r are new model parameters associated with the PSR. In order to make K_{pr} more sensitive to the stress ratio, ξ_r is usually larger than unity.

To complete the model, the definition of PSR loading rate $d\sigma_r$ is required. To determine $d\sigma_r$ in general stress space, it is first considered in the space with only x and y directions denoted as α. It can be expressed as $d\boldsymbol{\sigma}_r^{\alpha} = \mathbf{N}_r^{\alpha} d\boldsymbol{\sigma}$ and can be written in matrix form as:

$$\begin{pmatrix} d\sigma_{rx}^{\alpha} \\ d\sigma_{ry}^{\alpha} \\ d\sigma_{rxy}^{\alpha} \end{pmatrix} = \begin{bmatrix} \frac{1}{2} - \frac{(\sigma_x - \sigma_y)^2}{8t_J^{\alpha}} & -\frac{1}{2} + \frac{(\sigma_x - \sigma_y)^2}{8t_J^{\alpha}} & -\frac{(\sigma_x - \sigma_y)\sigma_{xy}}{2t_J^{\alpha}} \\ -\frac{1}{2} + \frac{(\sigma_x - \sigma_y)^2}{8t_J^{\alpha}} & \frac{1}{2} - \frac{(\sigma_x - \sigma_y)^2}{8t_J^{\alpha}} & \frac{(\sigma_x - \sigma_y)\sigma_{xy}}{2t_J^{\alpha}} \\ -\frac{(\sigma_x - \sigma_y)\sigma_{xy}}{4t_J^{\alpha}} & \frac{(\sigma_x - \sigma_y)\sigma_{xy}}{4t_J^{\alpha}} & 1 - \frac{\sigma_{xy}^2}{t_J^{\alpha}} \end{bmatrix} \begin{pmatrix} d\sigma_x \\ d\sigma_y \\ d\sigma_{xy} \end{pmatrix} \tag{15}$$

where $t_J^{\alpha} = (\sigma_x - \sigma_y)^2 / 4 + \sigma_{xy}^2$. Similarly, in the β space (y, z) and γ space (z, x), they can be defined as $d\boldsymbol{\sigma}_r^{\beta} = \mathbf{N}_r^{\beta} d\boldsymbol{\sigma}$ and $d\boldsymbol{\sigma}_r^{\gamma} = \mathbf{N}_r^{\gamma} d\boldsymbol{\sigma}$. Combining $d\boldsymbol{\sigma}_r^{\alpha}$, $d\boldsymbol{\sigma}_r^{\beta}$ and $d\boldsymbol{\sigma}_r^{\gamma}$ and letting $d\sigma_{rx} = d\sigma_{rx}^{\alpha} + d\sigma_{rx}^{\gamma}$, $d\sigma_{ry} = d\sigma_{ry}^{\alpha} + d\sigma_{ry}^{\beta}$ and $d\sigma_{rz} = d\sigma_{rz}^{\beta} + d\sigma_{rz}^{\gamma}$, $d\boldsymbol{\sigma}_r$ in the general stress space can be obtained as:

$$d\boldsymbol{\sigma}_r = \mathbf{N}_r d\boldsymbol{\sigma} \tag{16}$$

With the formulations derived above, the elastoplastic stiffness can be obtained. The total stress increment can be defined as:

$$d\boldsymbol{\sigma} = \mathbf{E}(d\boldsymbol{\varepsilon} - d\boldsymbol{\varepsilon}^p) = \mathbf{E}(d\boldsymbol{\varepsilon} - d\boldsymbol{\varepsilon}_m^p - d\boldsymbol{\varepsilon}_r^p) \tag{17}$$

$$E_{ijkl} = K\delta_{ij}\delta_{kl} + G(\delta_{ik}\delta_{jl} + \delta_{il}\delta_{jk} - 2/3\delta_{ij}\delta_{kl}) \tag{18}$$

where $\mathbf{E}$ is the elastic stiffness tensor. The tensor $\mathbf{N}_r$ plays the role of projecting the total stress rate onto the PSR direction and it has the following characteristics.

$$\mathbf{E}\,\mathbf{N}_r = 2G\,\mathbf{N}_r \tag{19}$$

From mathematical manipulations and equation (19), the relationship between the stress and strain rates can be expressed as:

$$d\boldsymbol{\sigma} = \mathbf{E}^{ep} d\boldsymbol{\varepsilon} \tag{20}$$

$$\mathbf{E}^{ep} = \mathbf{E} - B_1 \left[\frac{(\mathbf{ER})(\mathbf{IN}_r^*)}{K_{pr} + \mathbf{IN}_r^* \mathbf{R}_r} - \frac{(\mathbf{ER})(\mathbf{IE})}{K_{pr} + \mathbf{IER}_r} \right] - B_2 \left[\frac{(\mathbf{ER}_r)(\mathbf{IN}_r^*)}{\mathbf{IN}_r^* \mathbf{R}} - \frac{(\mathbf{ER}_r)(\mathbf{IE})}{K_p + \mathbf{IER}} \right] \tag{21}$$

$$\mathbf{N}_r^* = 2G\,\mathbf{N}_r \tag{22}$$

$$B_1 = \left(\frac{\mathbf{I}\mathbf{N}_r^* \mathbf{R}}{K_{pr} + \mathbf{I}\mathbf{N}_r^* \mathbf{R}_r} - \frac{K_p + \mathbf{I}\mathbf{E}\mathbf{R}}{K_{pr} + \mathbf{I}\mathbf{E}\mathbf{R}_r} \right)^{-1} \tag{23}$$

$$B_2 = \left(\frac{K_{pr} + \mathbf{I}\mathbf{N}_r^* \mathbf{R}_r}{\mathbf{I}\mathbf{N}_r^* \mathbf{R}} - \frac{K_{pr} + \mathbf{I}\mathbf{E}\mathbf{R}_r}{K_p + \mathbf{I}\mathbf{E}\mathbf{R}} \right)^{-1} \tag{24}$$

The above formulations show that the stiffness tensor is independent of stress increments and the stress and strain increments have a linear relationship, which indicates the easy numerical implementations. In these equations, if K_{pr} is set to be K_p and $\mathbf{R}_r$ to be $\mathbf{R}$, they will be downgraded to the formulations in the classical plasticity.

Three new model parameters related to the PSR are incorporated into the modified PSR model. They are h_{0r} and ξ_r for the plastic modulus and A_r for the flow rule. All of them are independent of the monotonic loading and can be easily calibrated through the pure rotational loading paths at different stress ratio levels. As the shear strain is not influenced by the dilatancy ratio, h_{0r} and ξ_r can be obtained first by the curves of shear stress-strain relationship fitting the test results. A_r can be obtained from the response between the other stress components and the volumetric strain.

4. Experimental Problems

4.1. Soil properties

In this research, three types of sands are used in a series of experimental tests. Leighton Buzzard sand (Fraction B) is used in the simulations of hollow cylinder tests from Yang [23] while Leighton Buzzard sand (Fraction E) is used in the simulations of the experimental tests from Visone [24]. Nevada sand No. 120 is used in the simulations of triaxial, torsional and rotational tests from Chen & Kutter [25].

Leighton Buzzard sand is quarried in and around Bedfordshire, Leighton Buzzard in the east of England. It consists of sub-rounded particles and contains mainly quartz [23]. The index properties of Leighton Buzzard sand (Fraction B & E) are listed in Table 1. Nevada No. 120 sand is uniform fine sand and its index properties are also summarized in Table 1 [25].

Table 1. Physical properties of Leighton Buzzard sand and Nevada sand [23-25].

Property	Leighton Buzzard sand (fraction B)	Leighton Buzzard sand (fraction E)	Nevada sand
Mean grain size D_{50}: mm	0.62	0.15	0.17
Uniformity coefficient C_u: D_{60}/ D_{10}	1.56	1.58	2.0
Specific gravity G_s	2.65	2.65	2.67
Minimum void ratio e_{min}	0.52	0.64	0.511
Maximum void ratio e_{max}	0.79	1.07	0.887

4.2. Problem definition

The original and modified PSR model will be implemented into the single element simulations of 3 sets of experimental tests by using a single element computer program. The experimental tests simulated are introduced here.

Firstly, a series of drained pure rotational shear tests with different stress ratios are simulated. These tests were conducted at the Nottingham Centre for Geomechanics (NCG) using the hollow cylinder test apparatus with Leighton Buzzard sand (Fraction B). Details of the material and these tests can be found in Yang [23]. The stress paths of these tests are illustrated in Figures 1-2 in the space of $\sigma_{\theta z}$ and σ_z-σ_θ (PSR space) because the pure rotation of principal stress can be presented clearly in this space. In these tests, specimens were firstly consolidated isotropically to an effective mean pressure p' of 200kPa. Then the effective mean stress p' and the intermediate principal stress parameter b were maintained at 200 kPa and 0.5, respectively. In drained pure rotational tests, the major principal stress direction was rotated at a slow rate of 2 degree/min to ensure the full drainage.

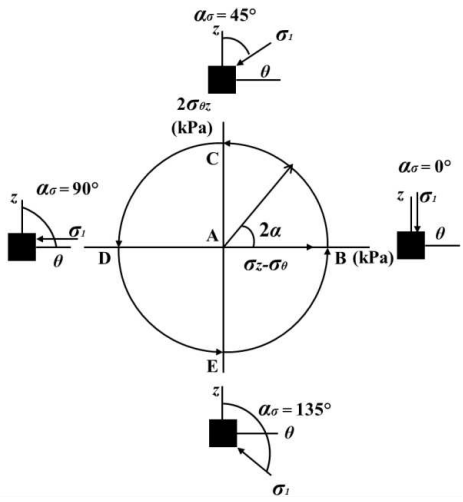

Figure 1. Stress paths of pure rotational loading in the PSR space for Leighton Buzzard sand (Fraction B) [23].

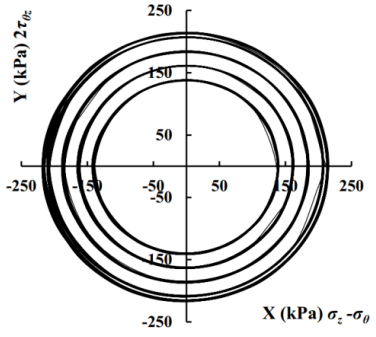

Figure 2. Actual stress paths of pure rotational loading with different stress ratios in the PSR space for Leighton Buzzard sand (Fraction B) [23].

Secondly, a series of drained triaxial tests using loose Leighton Buzzard sand (Fraction E) from Visone [24] are simulated. After the isotropic compressions, the tests were conducted by increasing or decreasing the axial stress with constant effective confining stress *p'* of 100 kPa and 200 kPa. As they do not involve the PSR, Triaxial tests are simulated to investigate the model capability under monotonic loading conditions and calibrate model parameters in this research.

Thirdly, a series of triaxial, torsional and rotational tests for Nevada sand from Chen & Kutter [25] are simulated. The stress paths of the undrained torsional and rotational tests are illustrated in Figure 3. The triaxial tests began with the isotropic initial condition. The mean confining pressure p was held constant during the shearing step of all the triaxial and hollow cylinder tests. In the undrained torsional shear tests, the axial loading was applied on the

isotropically consolidated sample until K = σ_θ/σ_z reached the desired value. The specimen was then subject to the cyclic shear stress. In the undrained rotational shear tests, the axial loading was also applied to the isotropically consolidated specimen before the rotational stress path in Figure 3 was performed.

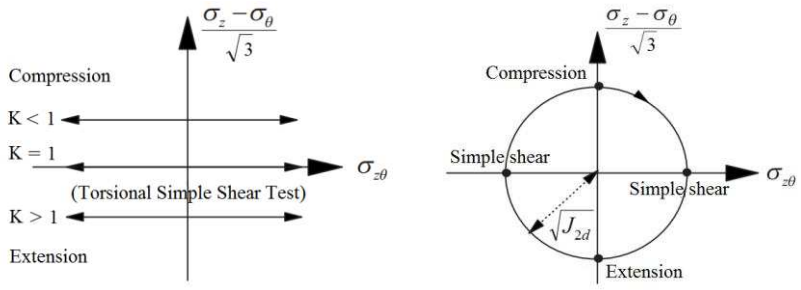

$$K = \frac{\sigma_\theta}{\sigma_z} \qquad \sqrt{J_{2d}} = \sqrt{\frac{(\sigma_z-\sigma_\theta)^2+3\sigma_{z\theta}^2}{3}} = \text{constant}$$

(a)

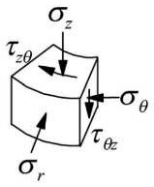

(b)

Figure 3. Stress paths for Nevada sand of undrained torsional shear tests (left) and undrained rotational shear tests (right) (a) and stress conditions (b) [25, 27].

5. Predicted Results and Comparison with the Experimental Data

5.1. Drained pure rotational shear tests for Leighton Buzzard sand (Fraction B)

A series of drained pure rotational shear tests are simulated using the original model and then the modified PSR model to test its ability in simulating PSR effects. The model parameters and initial conditions used in these simulations are listed in Table 2 and 3 respectively.

Table 2. Soil parameters of Leighton Buzzard sand (Fraction B), Leighton Buzzard sand (Fraction E) and Nevada sand.

	Constant	Parameters	Value (LBS B)	Value (LBS E)	Value (NS)
Original model	Elasticity	G_0	275	100	150
		v	0.25	0.25	0.25
	Critical state	M	1.07	1.35	1.45
		c	0.77	0.712	0.712
		λ_c	0.017	0.15	0.005
		e_0	0.77	0.977	0.807
		ξ	0.7	0.203	0.5
	Yield surface	m	0.014	0.013	0.05
	Plastic modulus	h_0	2.5	10	5.5
		c_h	0.868	0.968	0.968
		n^b	0.7	0.3	0.55
	Dilatancy	A_0	0.7	1.0	0.6
		n^d	0.3	0.1	3.5
Modified model	Plastic modulus	h_{0r}	2.27	3.3	0.9
		ξ^r	1.5	1.5	1.1
	Dilatancy	A_r	0.7	5.5	0.5

Table 3. Initial conditions of rotational shear tests for Leighton Buzzard sand (Fraction B) [23].

Relative density after consolidation (%)	Voil ratio after consolidation e_{con}	Stress ratio *q/p'*	Principal stress parameter b
75.9	0.585	0.6	0.5
75.9	0.585	0.8	0.5
75.9	0.585	0.93	0.5
75.9	0.585	0.97	0.5
76.6	0.583	1.02	0.5

The predicted and experimental results of rotational shear loadings with different stress ratios and cycles are shown in Figure 4. Figure 4(a) presents the results with stress ratios of 0.6, 0.8 and 0.93 for 5 cycles. It can be seen that in the early stage of rotational shear, the original model underestimates the volumetric strain in the case of *q/p'* = 0.93, while it significantly overestimates the volumetric strain in the case of *q/p'* = 0.8 & 0.6. This is mainly because the original model does not consider the PSR effect.

To better simulate this problem, the PSR model is used to simulate the same problem. It can be observed that in the simulation under same loading conditions, results from the modified PSR model show a significant difference compared to the original one. In the cases of *q/p'*=0.6 & 0.8, the modified PSR model generate less volumetric strain, which agrees better with the laboratory results. In the case of *q/p'*=0.93, which is close to the failure stress ratio, the results from the modified PSR model show larger volumetric contraction and fit the laboratory results well.

In the case of *q/p'*=0.97 from Figure 4(b), the experimental results show a dramatic contraction behavior after the principal stress direction rotates about 50 degrees. The numerical results show that the original model underestimates the volumetric contraction, especially for the dramatic increase of the volumetric contraction, while results from the modified model generally fit the experimental results better. In the case of *q/p'*=1.02, the experimental results show a dilative volumetric strain which may comes from the transportation of soil particles when their frictional forces fail to resist the large shear stress. The numerical results show that the modified model can reproduce this dilative behavior and its results generally fit the experimental results, while the results from the original model, however, still show a contractive behavior. An oscillating behavior is shown in both experimental and predicted results. This might come from the singularity problem of the modified model as a small yield surface and kinematic hardening is adopted, especially when the stress ratio is very high and close to the critical state, which is 1.07 [23].

It should be noted that the specimen fails earlier as the stress ratio approaches the critical value (1.07). This can be also seen from Figure 4(b) that in the cases with high stress ratios, the specimen fails within half a cycle.

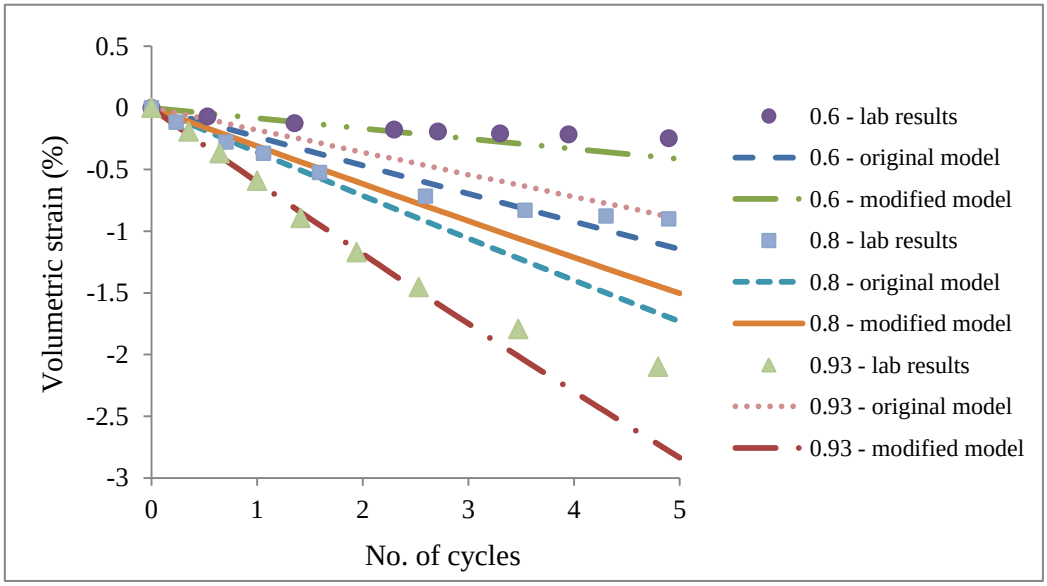

(a) stress ratio = 0.6, 0.8, 0.93 (5 cycles)

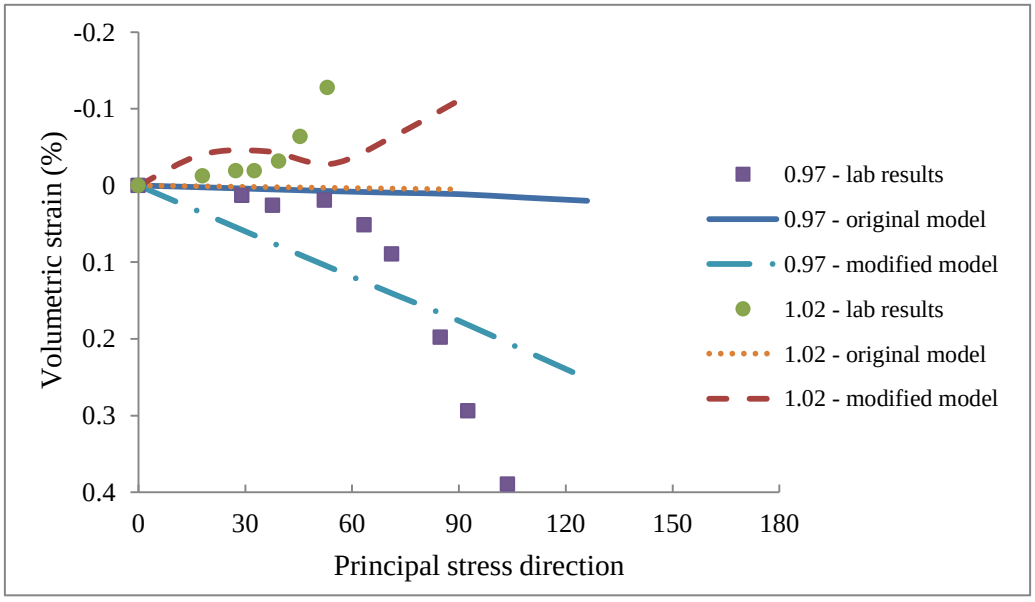

(b) stress ratio = 0.97, 1.02 (0.5 cycle)

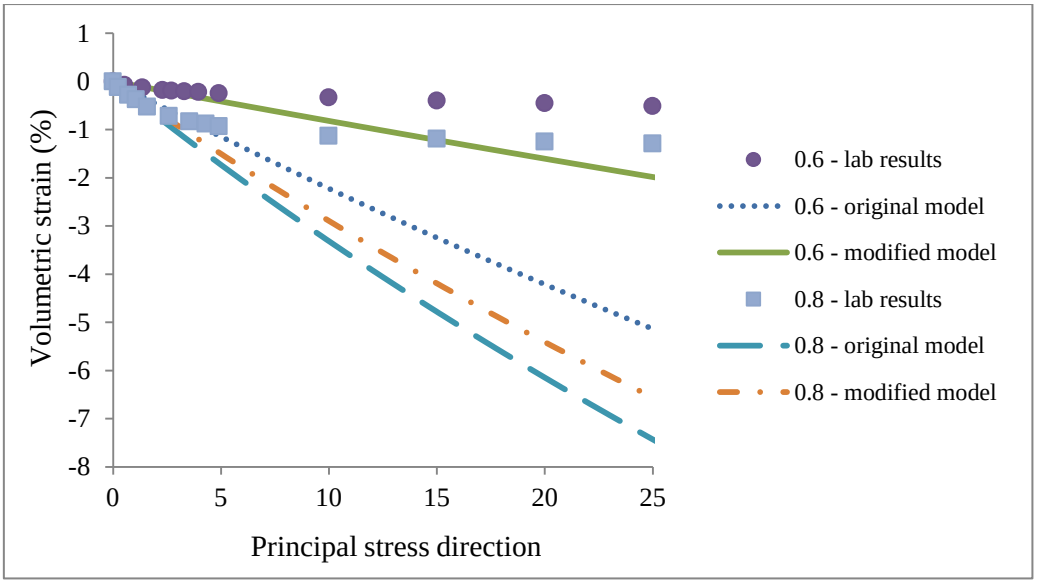

(c) stress ratio = 0.6, 0.8 (25 cycles)

Figure 4. Comparison of volumetric strain developments between the predicted results and laboratory results under the drained pure rotational loading for Leighton Buzzard sand (Fraction B).

Generally, results from the modified PSR model fit better with the laboratory results than the original model. However, in predicted and experimental results of 25 cycles from Figure 4(c), it can be seen that both the original model and modified model overestimates the volumetric strain after about 5 cycles. Experimental results in Figure 4 show a nonlinear trend and the volumetric compression tends to saturate, which are not seen in the predictions. The deviations come from the weakness of the PSR dilatancy mentioned after Equation 13. Both the original and modified models have no obvious mechanism to reproduce the saturation of compression after a large number of cycles of continuous PSR under drained conditions. Therefore, neither of them is suitable for the simulation of drained PSR loading at large cycles.

Despite this weakness, the PSR model is shown to be able to well reproduce the almost linear increase in volumetric strain in the early cycles, where most of the total volumetric strain is obtained. In conclusion, the results from these numerical simulations demonstrate that the modified PSR model performs better than the original model under the drained rotational loading conditions with the PSR.

5.2. Drained triaxial tests for Leighton Buzzard sand (Fraction E)

A series of triaxial tests with constant effective confining stress *p'* using loose Leighton Buzzard sand Fraction E (BS 100/170) from Visone [24] has also been simulated. All parameters are also listed in Table 2. Some typical results are shown in Figure 5.

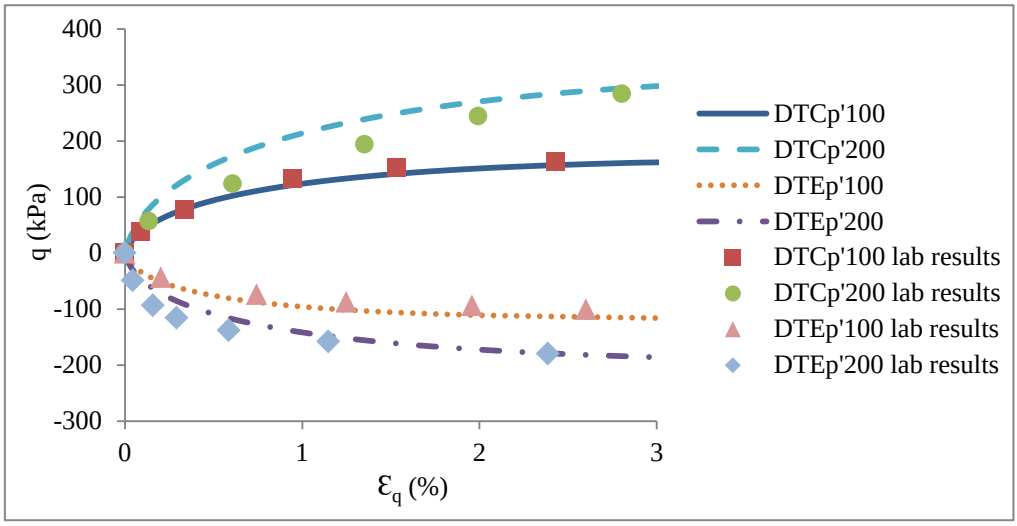

(a) Stress-strain responses

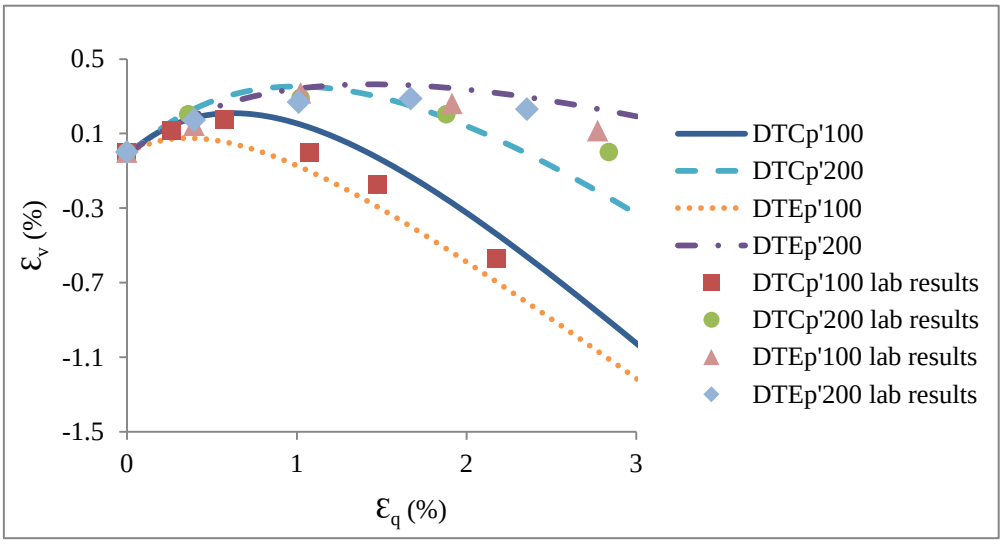

(b) Development of volumetric strain

Figure 5. Predicted results and test results of Leighton Buzzard sand (Fraction E) from drained triaxial tests with constant *p'* (100 & 200 indicate the confining pressure, C stands for compression while E stands for extension) [26].

Figure 5 show that the predicted results generally fit the lab results very well. There is no difference between the simulation results from the original model and the modified PSR model because all the tests are subjected to the monotonic loadings which do not involve the PSR effect.

5.3. Triaxial, torsional and rotational tests for Nevada sand

The original and PSR model are also used to simulate a series of triaxial, torsional and rotational tests for Nevada sand to investigate the significance of the PSR and test the ability of the PSR model in simulating the PSR impact and soil liquefaction. The triaxial tests do not have the PSR effect because of their monotonic loading path, while the torsional and rotational tests have the PSR effect. One set of model parameters listed in Table 2 are used for simulations of these tests. Some typical results are shown in Figures 6 to Figure 13.

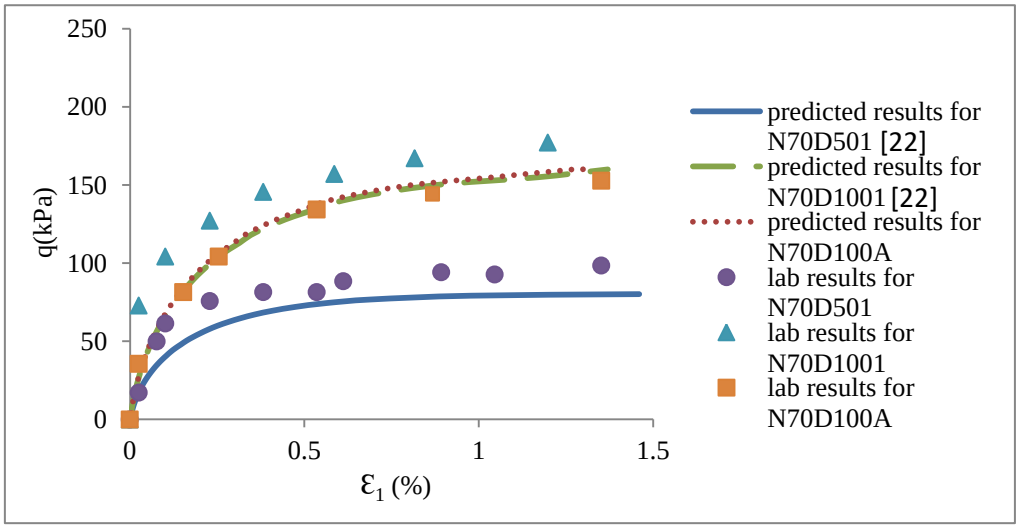

(a)

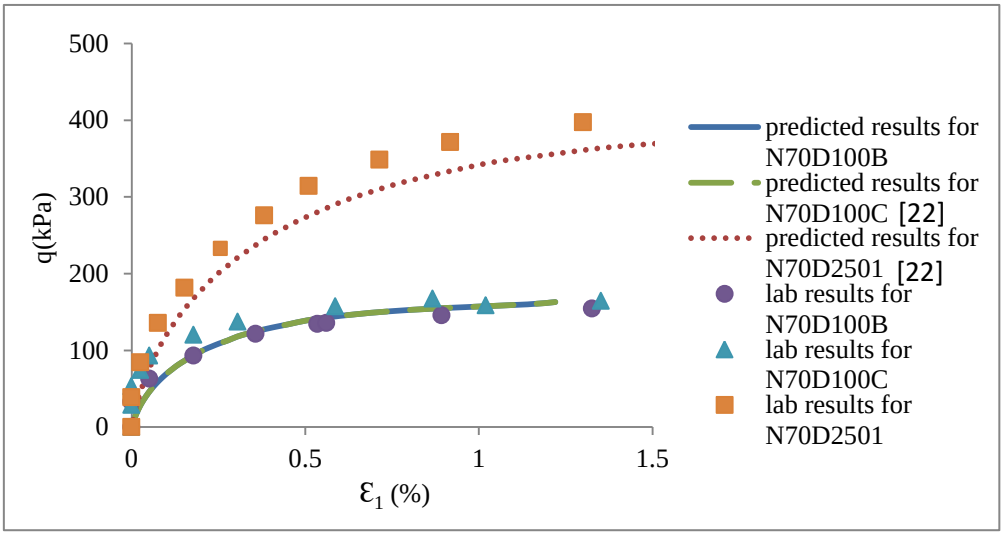

(b)

Figure 6. Test results and model predictions of stress-strain behaviors of drained monotonic loadings for Nevada sand.

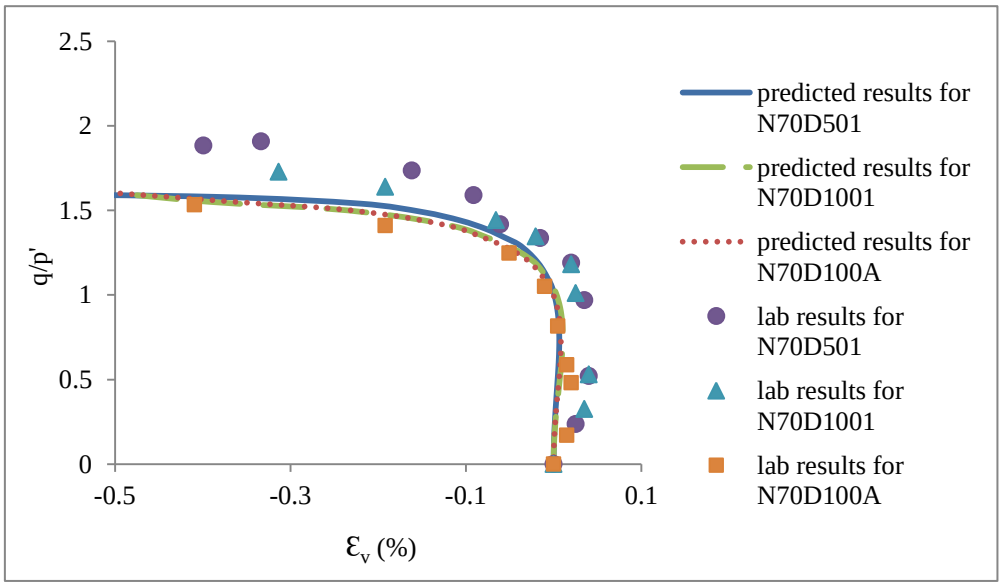

(a)

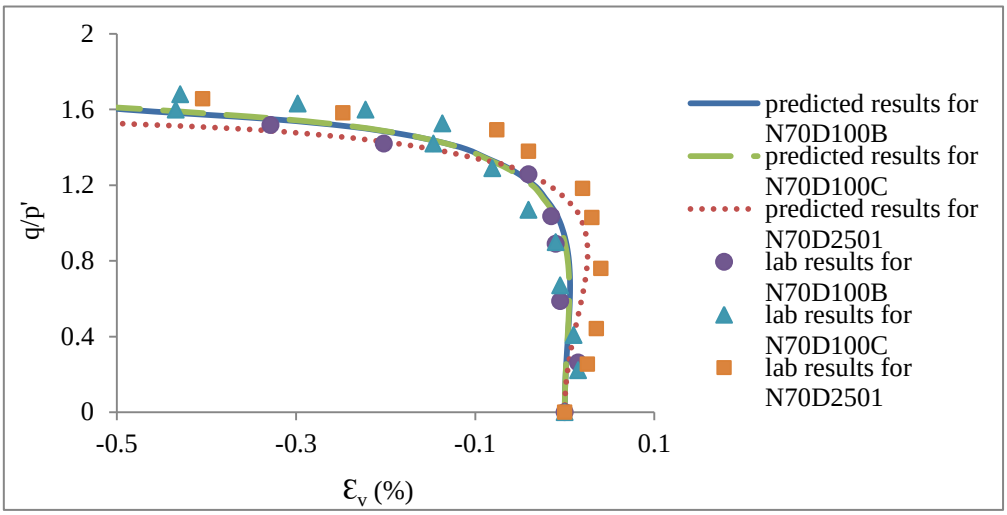

(b)

Figure 7. Test results and model predictions of relationships between stress ratios and volumetric strains of drained monotonic loadings for Nevada sand.

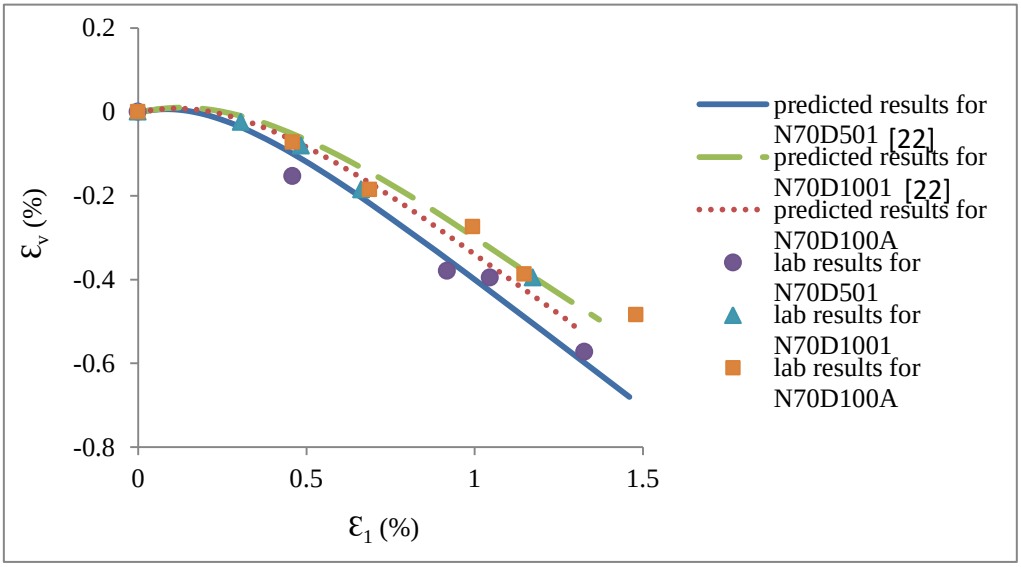

(a)

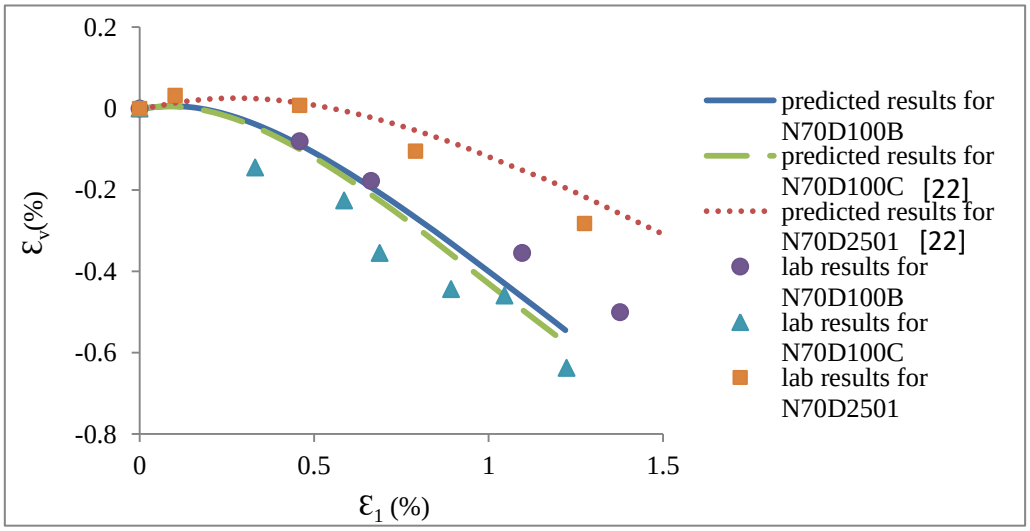

(b)

Figure 8. Test results and model predictions of volumetric strain behaviors of drained monotonic loadings for Nevada sand.

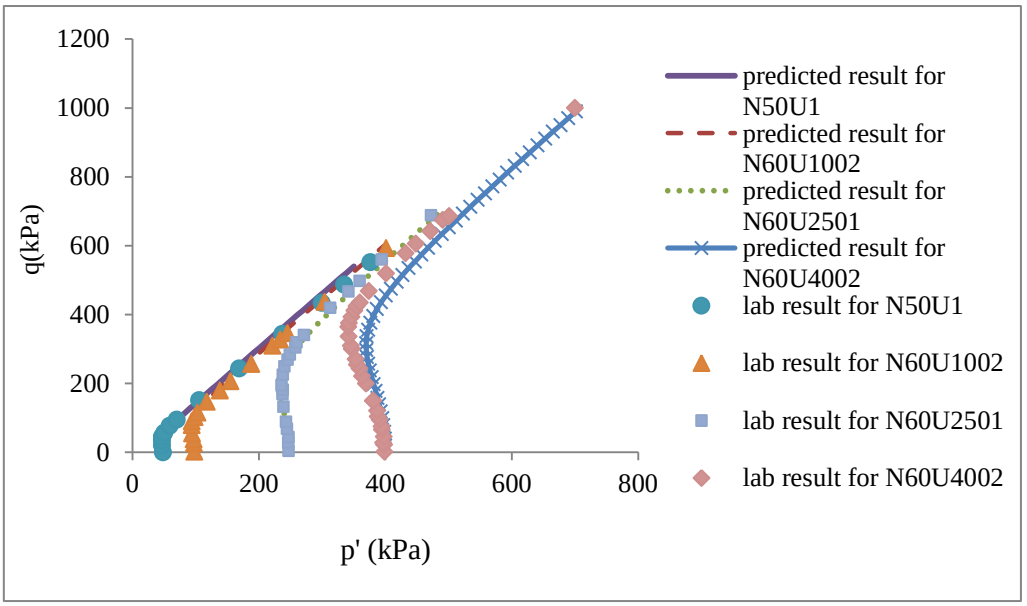

(a)

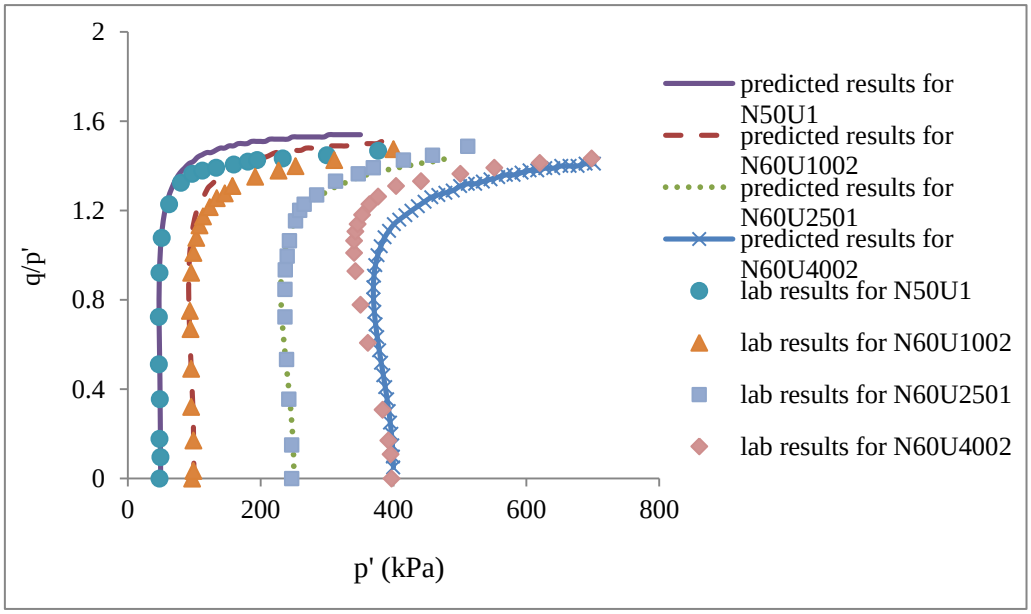

(b)

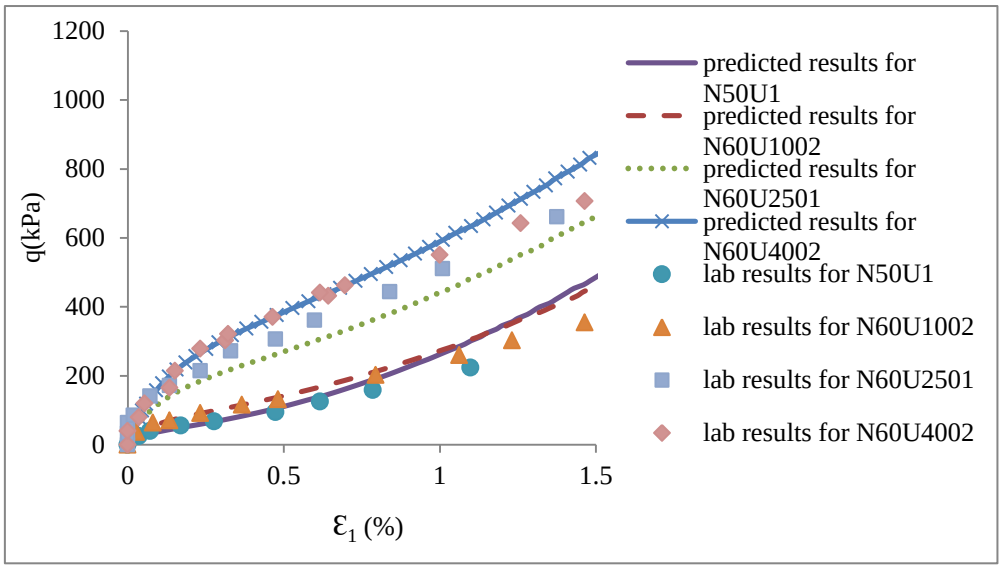

(c)

Figure 9. Test results and model predictions of undrained monotonic loadings for Nevada sand.

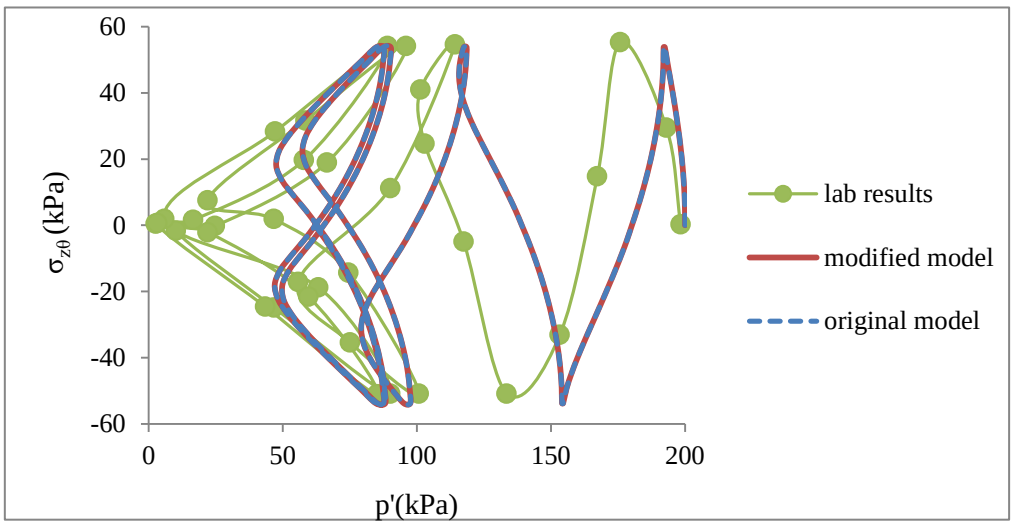

(a)

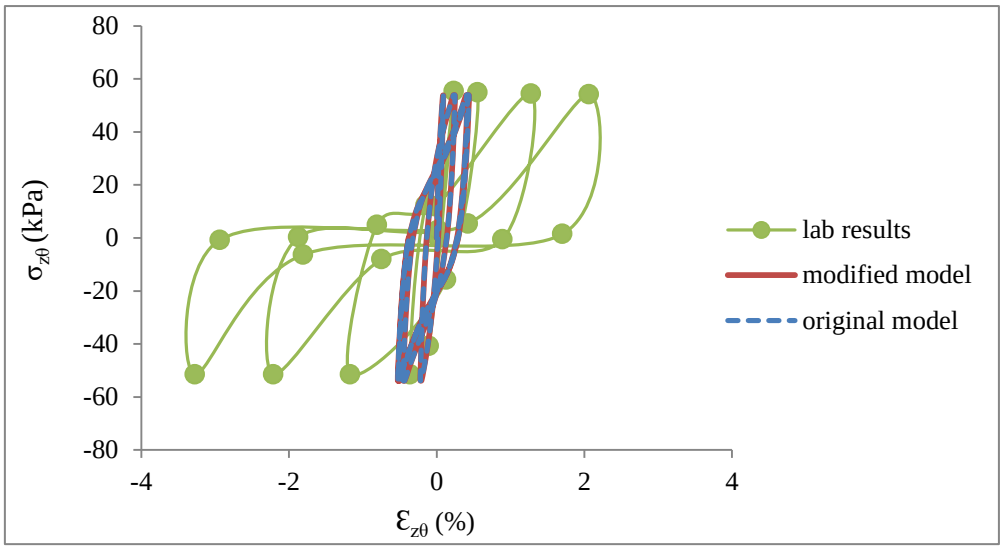

(b)

Figure 10. Test results and model predictions of torsional shear test NK10CU63 for Nevada sand.

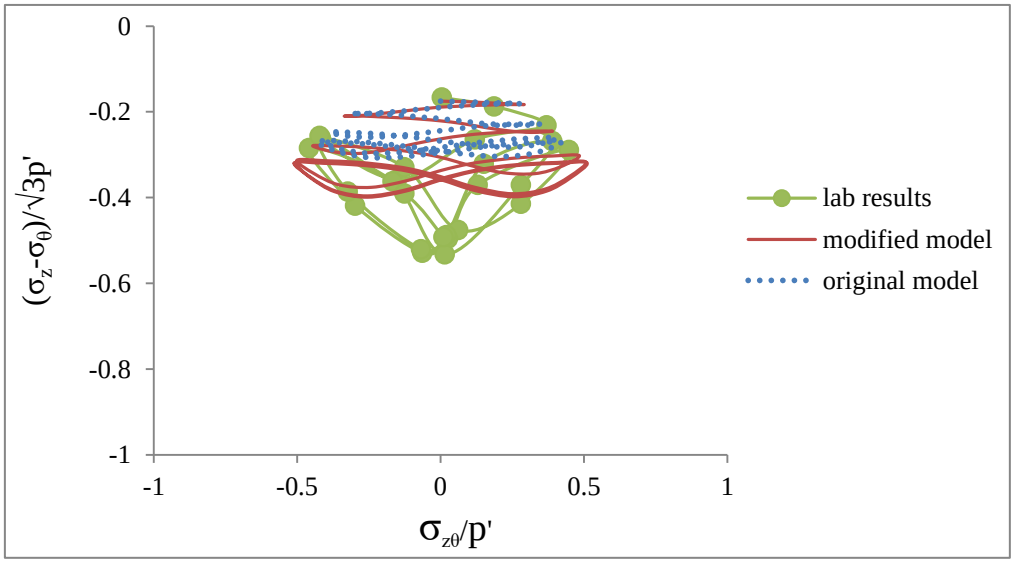

Figure 11. Test results and model predictions of torsional shear test NK138U51 for Nevada sand.

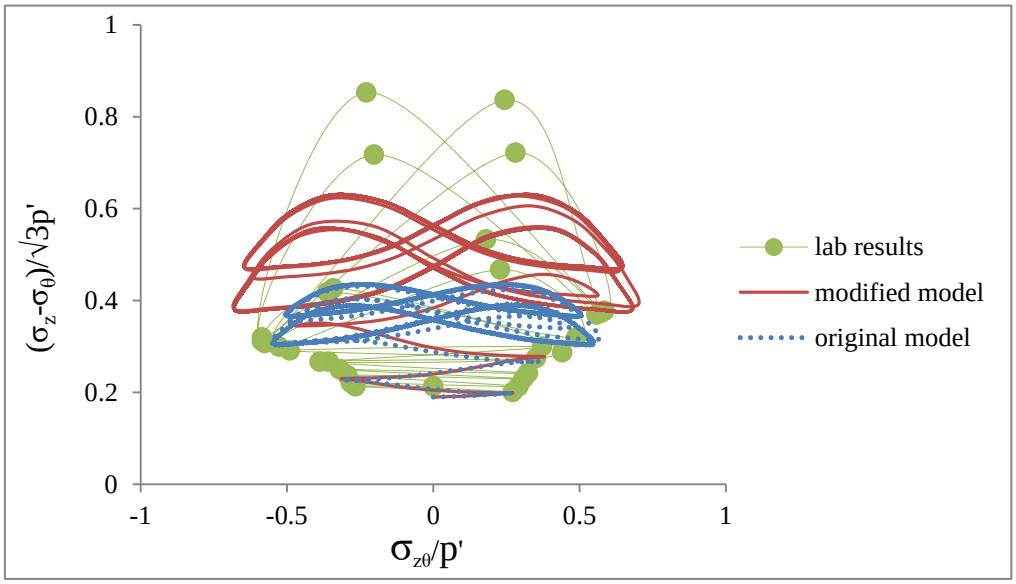

Figure 12. Test results and model predictions of torsional shear test NK73CU6 for Nevada sand.

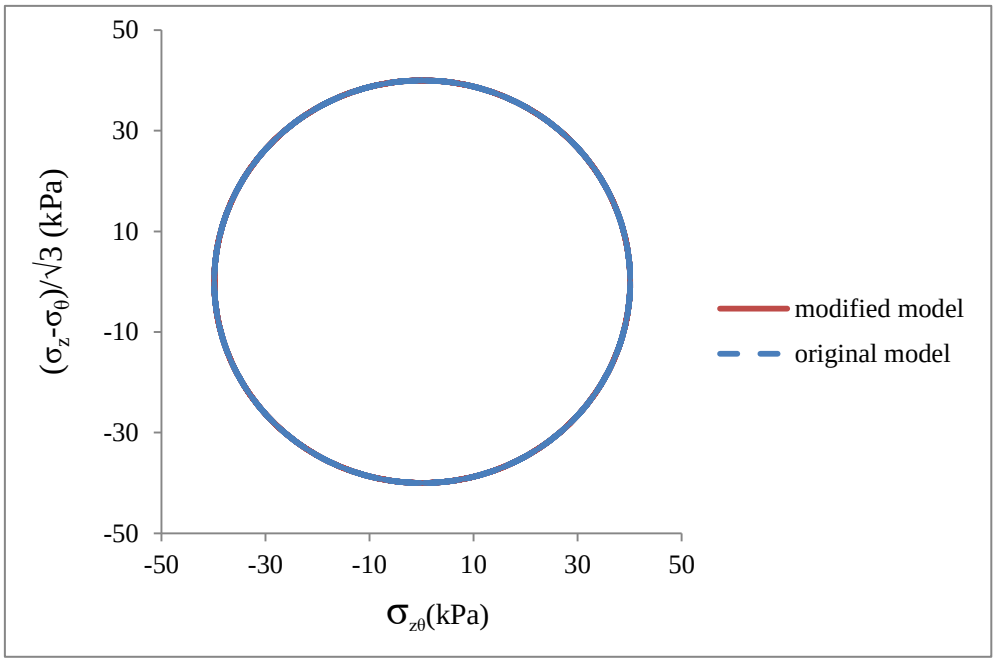
50
30
10
-10
-30
-50
-50
-30
-10
10
30
50
$(\sigma_z-\sigma_\theta)/\sqrt{3}$ (kPa)
$\sigma_{z\theta}$(kPa)
modified model
original model

(a)

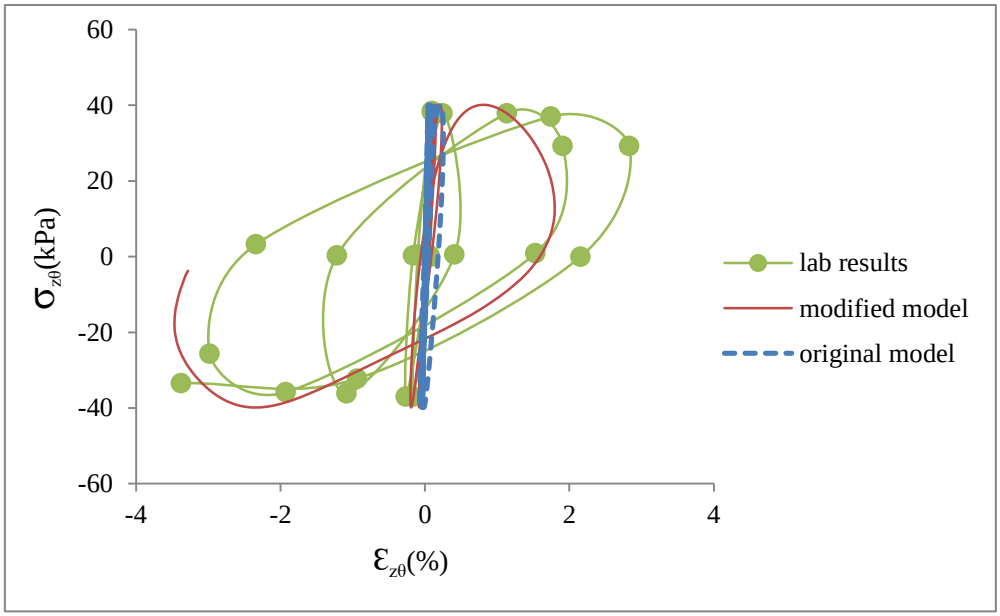
60
40
20
0
-20
-40
-60
-4
-2
0
2
4
$\sigma_{z\theta}$(kPa)
$\varepsilon_{z\theta}$(%)
lab results
modified model
original model

(b)

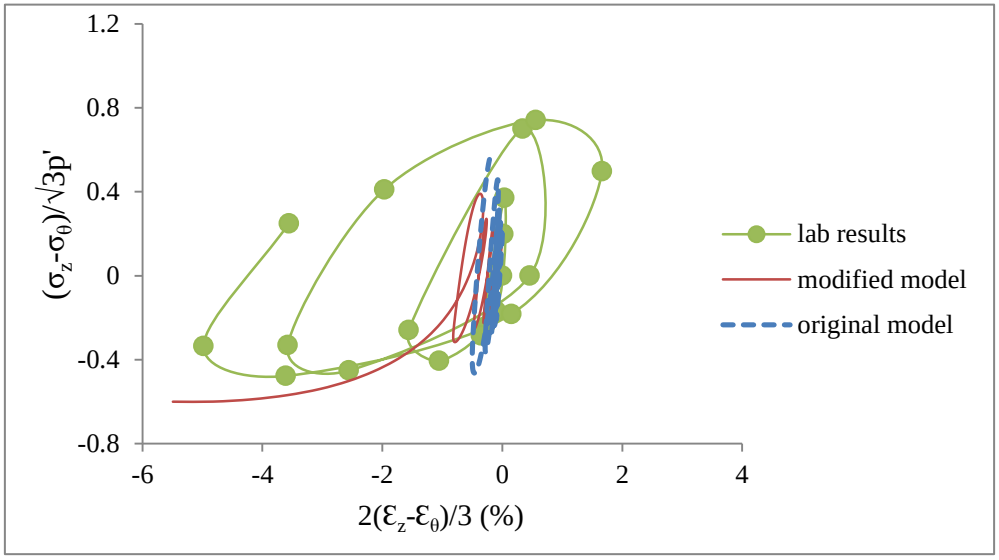

(c)

Figure 13. Test results and model predictions of rotational shear test NR40CU62 for Nevada sand.

The initial conditions of the drained and undrained tests are summarized in Table 4. Figure 6 to Figure 9 show the predicted results along with the experimental results. It can be seen that both the predictions for the drained and undrained tests generally fit the laboratory results very well. Therefore, this model has a good performance in reflecting soil behavior under drained monotonic loadings as well as the undrained monotonic loadings.

Table 4. Test conditions of drained and undrained triaxial tests for Nevada sand [25].

Specimen	Relative density (%)	Back pressure (kPa)	B value (%)	Initial confining pressure (kPa)
N70D501	74	250	98.1	50
N70D1001	72	250	98.6	100
N70D100A	76	200	100	100
N70D100B	82	200	98.3	100
N70D100C	85	200	99	100
N70D2501	75	250	99.1	250
N50U1	70	250	98.9	50
N60U1002	63	250	96	100
N60U2501	75	250	95.5	250
N60U4002	66	250	97.3	400

Table 5. Test conditions of torsioanl shear tests for Nevada sand [25].

Specimen	Relative density (%)	Back pressure (kPa)	B value (%)	Cell pressure (kPa)	K (σ_θ/σ_z)	Testing cycles
NK73CU6-1	68	100	97	213	0.73	12.5
NK73CU6-2	68	100	97	213	0.73	10
NK10CU63	65	100	100	300	1.0	4
NK138U51	71	200	99.2	400	1.38	4.75

The initial conditions of the torsional shear tests are summarized in Table 5 and Figure 10 to Figure 12 show the results of them. The predicted results of Test NK10CU63 in Figure 10 show that both the original model and modified PSR model underestimate the reduction of the effective confining pressure p' and the shear strain. This underestimation may also be resulted from the effect of fabric change. There is no difference between the predicted results from these two models because the principal stress does not rotate when K(σ_θ/σ_z) = 1.0. However, results from the modified PSR model show significant differences compared to the original model in Tests NK73CU6 and NK138U51 in which the value of K is not equal to 1.0 and the PSR effect is included.

The stress paths of $(\sigma_z-\sigma_\theta)/\sqrt{3}p'$ and $\sigma_{z\theta}/p'$ have been presented in Figure 11 & 12. The results from two models both show the reduction of effective confining pressure p' and the butterfly shape for stress paths because $\sigma_z-\sigma_\theta$ is held constant in the tests and the variation of $(\sigma_z-\sigma_\theta)/\sqrt{3}p'$ is due to the variation of p'. However, in the results from the original model the values of $(\sigma_z-\sigma_\theta)/\sqrt{3}p'$ stop reducing around -0.3 in NK138U51 and 0.42 in NK73CU6, which is significantly different from the laboratory results because the original model does not consider the PSR. In the results from the modified PSR model, the values of $(\sigma_z-\sigma_\theta)/\sqrt{3}p'$ reached about -0.4 in NK138U51 and 0.62 in NK73CU6, which agrees better with the laboratory results. The modified PSR model also predicts greater increasing of shear strain than the original model in the last cycles because of its consideration of PSR impacts.

The test conditions for the rotational shear test NR40CU62 are listed in Table 6 and the simulation results and experimental results are shown in Figure 13. It can be seen from Figure 13(a) that the stress paths from these two models are exactly the same, while the soil responses are quite different. In the rest of figures, the predicted results from the original model show very small shear strain and deviatoric strain. Therefore, the original model can only predict limited evolution of the shear strain of soil under undrained cyclic stress path including pure principal stress rotation and is unable to bring the soil to liquefaction, because it does not consider the PSR effect completely. However, in the predicted results from the modified PSR model, the maximum shear strain reached 5.5% with a dramatic increase in the

last cycle and brings the soil to the liquefaction as well. It should be noticed that although the computation ends when the shear strain reached 5.5% because of the instable condition and hard computation after the liquefaction, the general trends agrees well with the lab results (5%).

Table 6. Test conditions of the rotational shear rest for Nevada sand [25].

Specimen	Relative density (%)	Back pressure (kPa)	B value (%)	Cell pressure (kPa)
NR40CU62	67	100	99	300

6. Conclusion

This paper presents the application of a PSR model in the study of PSR effects on soil behaviors in a series of laboratory tests. The PSR model is developed on a base model with the bounding surface concept and soil critical state concept and the PSR induced stress rate is treated separately using an independent hardening and flow rule. The PSR model and the original model are used to study soil behavior in three sets of laboratory tests involving the PSR. In all the simulations, the predicted results from the models with and without considering PSR effects, as well as the experimental results have been compared to investigate the significance of PSR impact. The comparison generally show that the original model can only produce very limited p' reduction and cumulative shear strain under cyclic loading paths, thus significantly underestimates the soil liquefaction potential. On the other hand, under the same loading conditions, the predictions by the PSR model generates much larger reduction of p' and shear strains and can bring the soil to liquefaction. They agree better with the experimental results due to its complete ability in the simulation of the PSR impact. The results indicate the importance to independently consider the PSR and give special treatment of PSR for soil models in the simulation of these laboratory tests.

Acknowledgements

This research is supported by Zhejiang Natural Science Foundation (Project Code LQ19E090003), National Natural Science Foundation of China (NSFC Contract No. 51708040 & 11872219) and Lishui Major Research and Development (Project Code 2019ZDYF03). These supports are appreciated. The authors also acknowledge the support from the University of Lishui and University of Nottingham. Finally, the authors would like to greatly appreciate the anonymous reviewers for the valuable and in-depth comments.

References

[1] Ishihara K, Towhata I. Sand response to cyclic rotation of principal stress directions as induced by wave loads. Soils and Foundations 1983; 23(4): 11–26.

[2] Ishihara K, Yamazaki A. Analysis of wave-induced liquefaction in seabed deposits of sand. Soils and Foundations1984; 24(3): 85–100.

[3] Bhatia SK, Schwab J, Ishibashi I. Cyclic simple shear, torsional shear and triaxial—A comparative study. Proceedings of Advanced in the Art of Testing Soils under Cyclic Conditions, ASCE, New York 1985; 232–254.

[4] Miura K, Miura S, Toki S. Deformation behavior of anisotropic dense sand under principal stress axes rotation. Soils and Foundations 1986; 26(1): 36–52.

[5] Gutierrez M, Ishihara K, Towhata I. Flow theory for sand during rotation of principal stress direction. 1991; 31(4): 121–132.

[6] Li Y, Yang Y, Yu HS, Roberts G. Correlations between the stress paths of a monotonic test and a cyclic test under the same initial conditions. Soil Dynamics and Earthquake Engineering 2017; 101: 153–156.

[7] Rudnicki JW, Rice JR. Conditions for the localization of deformation in pressure-sensitive dilatant materials. Journal of Mechanics and Physics of Solids 1975; 23: 371–394.

[8] Wang ZL, Dafalias YF, Shen CK. Bounding surface hypoplasticity model for sand. Journal of Engineering Mechanics, American Society of Civil Engineers 1990; 116 (5): 983–1001.

[9] Kolymbas D. An outline of plasticity. Archive of Applied Mechanics 1991; 61: 143–151.

[10] Iai S, Matsunaga Y, Kameoka T. Strain space plasticity model for cyclic mobility. Soils and Foundations 1992; 32(2): 1–15.

[11] Fang HL. A state-dependent multi-mechanism model for sands. Geotechnique 2003; 53(4): 407–420.

[12] Li XS, Dafalias YF. A constitutive framework for anisotropic sand including non-proportional loading. Geotechnique 2004; 54(1): 41–55.

[13] Yu HS, Yuan X. On a class of non-coaxial plasticity models for granular soils. Proceedings of the Royal Society A – Mathematical Physical and Engineering Sciences 2005; 462 (2067): 725–748.

[14] Chang KT, Sture S. Microplane modeling of sand behavior under non-proportional loading. Computers and Geotechnics 2006; 33: 177–187.

[15] Yao YP, Hou w, Zhou A. UH model: three-dimensional unified hardening model for overconsolidated clays. Geotechnique 2009; 59(5): 451–469.

[16] Yao YP, Tian Y, Gao Z. Anisotropic UH model for soils based on a simple transformed stress method. International Journal for Numerical and Analytical Methods in

Geomechanics 2016; 41(1): 54–78.
[17] Tian Y, Yao YP. Modelling the non-coaxiality of soils from the view of cross-anisotropy. Computers and Geotechnics 2017; 86: 219–229.
[18] Gutierrez M, Ishihara K, Towhata, I. Model for the deformation of sand during rotation of principal stress directions. Soils and Foundations 1993; 33(3): 105–117.
[19] Yang Y, Yu HS. A kinematic hardening soil model considering the principal stress rotation. International Journal for Numerical and Analytical Methods in Geomechanics 2013; 37: 2106–2134.
[20] Dafalias YF, Manzari MT. Simple plasticity sand model accounting for fabric change effects. Journal of Engineering Mechanics, ASCE 2004; 130(6): 622–634.
[21] Lashkari A, Latifi M. A non-coaxial constitutive model for sand deformation under rotation of principal stress axes. International Journal for Numerical and Analytical Methods in Geomechanics 2008; 32: 1051–1086.
[22] Petalas AL, Dafalias YF, Papadimitriou AG. SANISAND-FN: An evolving fabric-based sand model accounting for stress principal axes rotation. International Journal for Numerical and Analytical Methods in Geomechanics 2018; 1–27.
[23] Yang L. Experimental Study of Soil Anisotropy Using Hollow Cylinder Testing. PhD Thesis, University of Nottingham, UK 2013.
[24] Visone C. Performance-based approach in seismic design of embedded retaining walls. PhD thesis, University of Napoli Federico II, Napoli, Italy 2008; Annex A1–A21.
[25] Chen YR, Kutter BL. Contraction, dilation and failure of sand in triaxial, torsional and rotational shear tests. Journal of engineering mechanics 2009; 135(10): 1155–1165.
[26] Wang Z, Yang Y, Yu HS. Effects of principal stress rotation on the wave–seabed interactions. Acta Geotechnica 2016; 12(1): 97–106.
[27] Wang Z, Yang Y, Yu HS, Muraleetharan, KK. Numerical simulation of earthquake-induced liquefactions considering the principal stress rotation. Soil Dynamics and Earthquake Engineering 2016; 90: 432–441.

Table and Figure Captions

Table 1. Physical properties of Leighton Buzzard sand and Nevada sand [23-25].

Table 2. Soil parameters of Leighton Buzzard sand (Fraction B), Leighton Buzzard sand (Fraction E) and Nevada sand.

Table 3. Initial conditions of rotational shear tests for Leighton Buzzard sand (Fraction B) [23].

Table 4. Test conditions for drained and undrained triaxial tests for Nevada sand [25].

Table 5. Test conditions of torsioanl shear tests for Nevada sand [25].